



**HAL**  
open science

# Revisiting the formation mechanism of intragranular $\kappa$ -carbide in austenite of a Fe-Mn-Al-Cr-C low-density steel

Jianlei Zhang, Yueshan Jiang, Weisen Zheng, Yuxiang Liu, Ahmed Addad, G Ji, Changjiang Song, Qijie Zhai

## ► To cite this version:

Jianlei Zhang, Yueshan Jiang, Weisen Zheng, Yuxiang Liu, Ahmed Addad, et al.. Revisiting the formation mechanism of intragranular  $\kappa$ -carbide in austenite of a Fe-Mn-Al-Cr-C low-density steel. Scripta Materialia, 2021, Scripta Materialia, 199, pp.113836. 10.1016/j.scriptamat.2021.113836 . hal-03323667

**HAL Id: hal-03323667**

**<https://hal.science/hal-03323667>**

Submitted on 22 Aug 2021

**HAL** is a multi-disciplinary open access archive for the deposit and dissemination of scientific research documents, whether they are published or not. The documents may come from teaching and research institutions in France or abroad, or from public or private research centers.

L'archive ouverte pluridisciplinaire **HAL**, est destinée au dépôt et à la diffusion de documents scientifiques de niveau recherche, publiés ou non, émanant des établissements d'enseignement et de recherche français ou étrangers, des laboratoires publics ou privés.

# 1 Revisiting the formation mechanism of intragranular 2 $\kappa$ -carbide in austenite of a Fe-Mn-Al-Cr-C 3 low-density steel

4 Jianlei Zhang<sup>a, b, c</sup>, Yueshan Jiang<sup>b</sup>, Weisen Zheng<sup>b</sup>, Yuxiang Liu<sup>a, b</sup>, Ahmed Added<sup>c</sup>, Gang Ji<sup>c\*</sup>,  
5 Changjiang Song<sup>a, b\*</sup>, Qijie Zhai<sup>a, b</sup>

6 <sup>a</sup> Center for Advanced Solidification Technology (CAST), School of Materials Science and  
7 Engineering, Shanghai University, Shanghai 200444, China

8 <sup>b</sup> State Key Laboratory of Advanced Special Steel, School of Materials Science and  
9 Engineering, Shanghai University, Shanghai 200444, China

10 <sup>c</sup> Univ. Lille, CNRS, INRAE, Centrale Lille, UMR 8207 - UMET - Unité Matériaux et  
11 Transformations, F-59000 Lille, France

12 \*Corresponding author:

13 Gang Ji: [gang.ji@univ-lille.fr](mailto:gang.ji@univ-lille.fr);

14 Changjiang Song: [riversong@shu.edu.cn](mailto:riversong@shu.edu.cn).

## 16 Abstract

17 It was usually believed that the formation of intragranular  $\kappa$ -carbide in  $\gamma$ -austenite  
18 was attributed to spinodal decomposition followed by ordering reaction. In this work,  
19 near-atomic scale characterization of an austenite-based Fe-20Mn-9Al-3Cr-1.2C  
20 (wt. %) low-density steel, using (high-resolution) scanning transmission electron  
21 microscopy and atomic probe tomography, reveals that the initially-formed  $\kappa$ -carbides  
22 (2-3 nm in particle size) are featured with an ordered L'1<sub>2</sub> structure but without  
23 detectable chemical partitioning. Further, the Gibbs energy of the FCC phase obtained  
24 by thermodynamic calculations always shows a positive curvature (i.e.  $\frac{d^2G}{dx^2} < 0$ ) with  
25 the variable contents of Al and C in the temperature range 400-800 °C. Both the  
26 results demonstrate that the ordered nuclei of  $\kappa$ -carbide can form directly in the  
27 disordered  $\gamma$ -austenite rather than through the well-known spinodal  
28 decomposition-ordering mechanism. The extremely low nucleation barrier is due to  
29 the similar lattice structure, same composition and complete coherency between the  
30  $\gamma$ -austenite matrix and  $\kappa$ -carbides.

31 **Keywords:** Low-density steel,  $\kappa$ -carbide, Spinodal decomposition, Atom probe  
32 tomography (APT), Thermodynamic calculation.

33  
34 Precipitation strengthening promoted by nano-scale  $\kappa$ -carbides in austenite-based

35 Fe-Mn-Al-C low-density steels has received much attention since such shearable and  
36 coherent precipitates within the  $\gamma$ -austenite matrix significantly enhance strength  
37 without sacrificing too much elongation [1-6]. The ideal stoichiometry of  
38 intragranular  $\kappa$ -carbide is  $(\text{Fe, Mn})_3\text{AlC}$ , and it has a perovskite crystal structure  
39 designated as  $E2_1$  in the Strukturbericht classification [1]. Based on observations of  
40 electron diffraction patterns and calculations of structure factors, an elemental  
41 site-occupancy in the  $\kappa$ -carbide was summarized as that Fe and Mn atoms were  
42 located at face center positions, Al atoms at corner positions, and C atom at body  
43 center octahedral ( $\frac{1}{2}, \frac{1}{2}, \frac{1}{2}$ ) interstitial position of this structure [1, 7, 8]. It was  
44 reported that the  $\kappa$ -carbide could initially form at the solid solution state [4, 9-11], and  
45 its coarsening occurred during isothermal aging treatments in the temperature range  
46 450-600 °C [1, 12-14].

47 It has long been believed that in most austenite matrix alloys, the formation of  
48 intragranular  $\kappa$ -carbide is through spinodal decomposition and following ordering  
49 reaction [1, 15, 16]. Its formation sequence is generally described as follows [1]: a  
50 spinodal decomposition divides high temperature  $\gamma$ -austenite into the solute-lean (C  
51 and/or Al) phase  $\gamma'$  and the solute-rich phase  $\gamma''$ ; then the solute-rich phase  $\gamma''$   
52 transforms into the ordered  $L1_2$  phase, in which Al and Fe/Mn atoms are located at  
53 corner and face center sites, respectively; finally, the  $\kappa$ -carbide with  $E2_1$  structure  
54 forms by further ordering of C atoms. Usually, the non-stoichiometric  $\kappa$ -carbide ( $(\text{Fe,}$   
55  $\text{Mn})_3\text{AlC}_x$ ) is observed being referred as  $L'1_2$  ordered phase.

56 In the early years, conventional transmission electron microscopy (TEM) and  
57 X-ray diffraction (XRD) were used as the main tools to provide experimental  
58 evidence supporting the spinodal decomposition-ordering mechanism by observing  
59 the modulated structure [17], diffuse satellites around the (020) diffraction spots in  
60 electron diffraction patterns and XRD sideband peaks around the (200) reflections [16,  
61 18]. Over recent years, the composition uncertainty of  $\kappa$ -carbide was quantitatively  
62 resolved at near-atomic scale by atom probe tomography (APT) [4, 7, 12]. The  
63 concentration profiles with sinusoidal curves across the  $\gamma$ -austenite matrix and  
64 developed  $\kappa$ -carbide were found to confirm the occurrence of spinodal decomposition  
65 during  $\kappa$ -carbide precipitation [12, 19].

66 However, very recent TEM and APT results obtained in a Fe-30Mn-9Al-1.2C  
67 (wt. %) lightweight steel surprisingly indicated that the formation of an ordered  
68 structure was earlier than chemical partitioning of any solute elements during the  
69 early stage of  $\kappa$ -carbide precipitation [4]. This observation obviously challenged the  
70 general understanding of the  $\kappa$ -carbide formation process. In fact, the study of  
71  $\kappa$ -carbide mainly focused on the coarsened  $\kappa$ -carbide at the aged states where both  
72  $L'1_2$  ordered structure and chemical partitioning were observed. Comparatively, the

73 study of the  $\kappa$ -carbide formation at the initial stage is still very limited due to tiny size  
74 of  $\kappa$ -carbide in the range of a few nanometers and complete coherency with  
75  $\gamma$ -austenite. Therefore, the understanding of  $\kappa$ -carbide formation process at the initial  
76 stage has still been insufficient. The objective of this work is to revisit the formation  
77 mechanism of  $\kappa$ -carbide in an austenite-based Fe-20Mn-9Al-3Cr-1.2C (wt. %)   
78 low-density steel at near-atomic scale by probe-corrected (high-resolution) scanning  
79 TEM ((HR)STEM), APT and thermodynamic calculation.

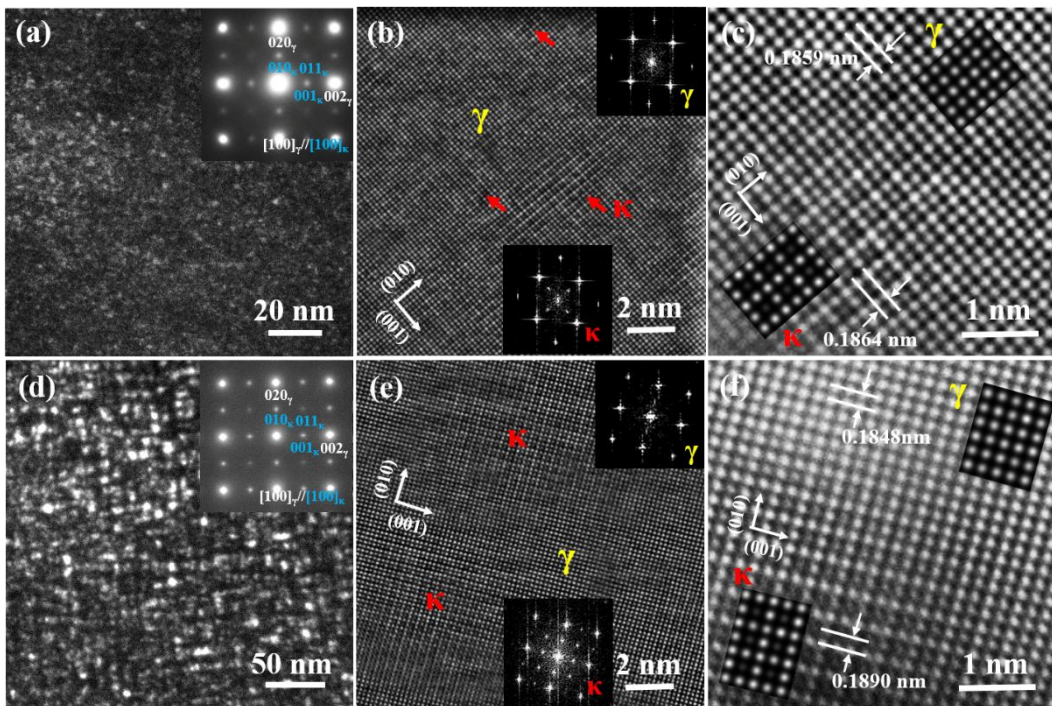
80 As detailed in our previous works [9, 20], the steel sample was prepared by  
81 centrifugal casting under near-rapid solidification in an argon atmosphere. Molten  
82 metal was poured directly into a copper mold and solidified at a cooling rate higher  
83 than  $10^3$  K/s [21]. Isothermal aging was carried out under vacuum at 600 °C for 9 h,  
84 followed by furnace cooling. Chemical composition of the as-cast steel, measured by  
85 an inductively coupled plasma-atomic emission spectrometry (ICP-AES) and a  
86 carbon-sulfur analyzer (CS2800), was Mn 19.70 wt. %, Al 8.86 wt. %, Cr 2.90 wt. %,   
87 C 1.21 wt. % and Fe balance.

88 TEM examination was carried out using a FEI Tecnai G2-20 twin and a  
89 Thermofisher Titan Themis 300 microscopes, operated at 200 and 300 kV,  
90 respectively. The latter was equipped with a probe aberration corrector allowing to  
91 acquire (HR)STEM images. The probe size was set to 0.1 nm with a convergence  
92 semi-angle of 22.5 mrad. Collection angle of the high-angle annular dark-field  
93 (HAADF) imaging detector was in the range 80-150 mrad. TEM specimens were  
94 prepared by twin-jet electrolytic polishing at -30 °C and 30 V, with a mixed solution  
95 of 10 % perchloric acid and 90 % alcohol. Dr. probe software was used for  
96 atomic-scale HAADF image simulation [22]. Standard two-step electro-polishing was  
97 used to prepare needle-like specimens for APT using a local electrode atom probe  
98 instrument (CAMECA LEAP 4000 XHR), in laser-pulsing mode with a repetition rate  
99 of 200 kHz, a pulse fraction of 15 %, and a specimen temperature of 50 K.  
100 Post-treatment of APT data was done using IVAS 3.6.8 software (CAMECA software  
101 suite). The peak decomposition algorithm in IVAS was used to resolve the peak  
102 overlaps among Fe, Al and Cr at 27 Da in mass spectrum, which has been proven to  
103 significantly improve counting statistics [23, 24].

104 Thermodynamic calculations were performed by Thermo-Calc software using  
105 previously-created thermodynamic database of low-density steels [25-29].  
106 Partitioning model based on the Compound Energy Formalism (CEF) was employed  
107 to describe disordered and ordered forms (such as  $L1_2$  and  $L1_0$ ) of the FCC phase in  
108 the database and the detailed calculation process was given in [Supplementary](#).

109 The DF-TEM images (in Fig. 1 (a) and (d)) show that the homogeneously

110 dispersed  $\kappa$ -carbide precipitates are present at the as-cast and aged states, and have the  
 111 average sizes of around 3 and 10 nm, respectively. Being consistent with the previous  
 112 results [1], the selected area diffraction patterns (SADPs, insets in Fig. 1 (a) and (d))  
 113 show that the  $\kappa$ -carbides have a cube-on-cube orientation relationship with the  
 114  $\gamma$ -austenite:  $[100]_{\kappa} // [100]_{\gamma}$  and  $(100)_{\kappa} // (100)_{\gamma}$ . By measuring the  $\{100\}$  and  $\{110\}$   
 115 superlattice reflection intensity in SADP shown in Fig. 1 (a) and (d), the intensity  
 116 ratios of  $I_{(011)}/I_{(001)}$  in the as-cast and aged samples are 0.52 and 0.25, respectively.  
 117 This suggests that the ordering of C atoms in the body-center octahedral sites is  
 118 gradually improved with the growth of  $\kappa$ -carbides. It was reported that the intensity of  
 119 the  $\{100\}$  superlattice spots is higher than the  $\{110\}$  ones in  $L'1_2$  structure [17, 30,  
 120 31]. Since theoretically the intensity of the superlattice reflections is proportional to  
 121 square of the structure factor ( $F_{hkl}$ ,  $h$ ,  $k$  and  $l$  are the Miller indices), the  $L'1_2$  structure  
 122 with partially C ordering can be distinguished [32]. Contrasts in an HAADF image is  
 123 proportional to  $Z^{-1.7-2}$  [33], meaning that the bright contrast indicates Cr- ( $Z=24$ ), Mn-  
 124 ( $Z=25$ ) and/or Fe-rich ( $Z=26$ ) atomic columns, while dark contrast represents Al-  
 125 ( $Z=13$ ) and/or C-rich ( $Z=6$ ) atomic columns in this case. Thus, the individual  
 126  $\kappa$ -carbide precipitates can be identified using FFT patterns shown in Fig. 1 (b) and (e),  
 127 which have the fully coherent interface with the  $\gamma$ -austenite matrix and no interfacial  
 128 misfit dislocation is visible. Although the exact atomic occupations of Cr and Mn are  
 129 unknown, the contrasts of the  $\kappa$ -carbides approximately correspond to those of the  
 130 simulation results using the  $E2_1$  structural model shown in Figs. 1 (c) and (f).

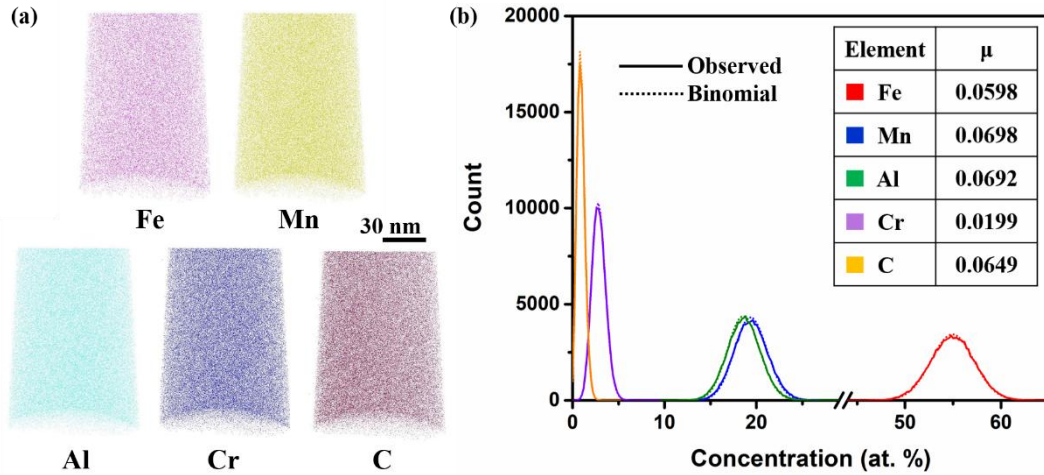


131

132

Fig. 1 (HR)(S)TEM characterization of the as-cast (a-c) and aged steels (d-f): (a) and (d) are

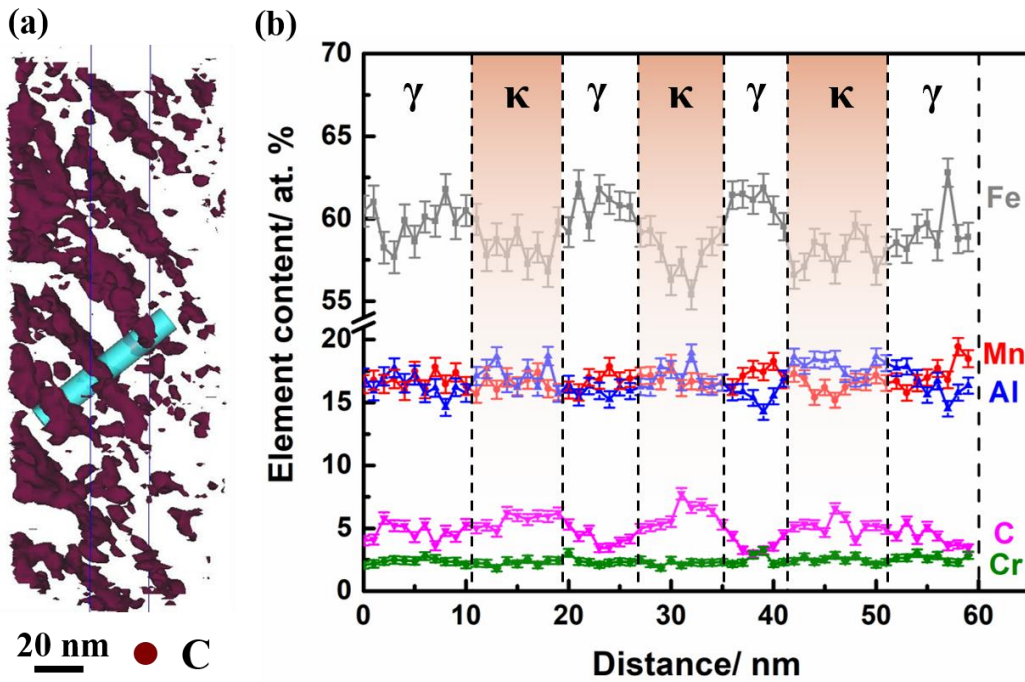
133 dark-field (DF) TEM images, insets are corresponding SADP of  $[100]_{\gamma}$  zone-axis; (b) and (e) are  
 134 filtered HRSTEM-HAADF images along  $[100]_{\gamma}$  zone axis, insets are corresponding *fast Fourier*  
 135 *transform* (FFT) patterns of  $\gamma$ -austenite and  $\kappa$ -carbide; (c) and (f) are zoom-in images of (b) and (e)  
 136 respectively, overlapped images are simulated HRSTEM-HAADF images using  $\kappa$ -carbide ( $E2_1$   
 137  $Fe_3AlC$ ) and  $\gamma$ -austenite (FCC Fe) structure models.



138  
 139 Fig. 2 APT characterization of  $\gamma$ -austenite in the as-cast steel: (a) Fe, Mn, Al, Cr and C elemental  
 140 maps; (b) frequency distribution analysis obtained by comparing the observed experimental results  
 141 and the binomial simulation, and the values of normalized homogenization parameter  $\mu$  are listed  
 142 in the inserted table in (b).

143 The APT result in Fig. 2 (a) shows that the distributions of all the five solute  
 144 elements (Fe, Mn, Al, C and Cr) are visibly uniform in  $\gamma$ -austenite of the as-cast steel.  
 145 According to the TEM-DF image shown in Fig. 1 (a), the density of the  $\kappa$ -carbides  
 146 with a size of 3 nm is almost  $3/100 \text{ nm}^2$ . It is estimated to have at least 294 observable  
 147  $\kappa$ -carbide particles in the 2-dimensional surface of the APT-reconstructed map if  
 148 chemical ordering exists. However, no chemical partitioning caused by the formation  
 149 of tiny  $\kappa$ -carbides (confirmed by TEM in Fig. 1 (a-c)) is detected. As shown in Fig. 2  
 150 (b), the observed data (solid line) fit with the binomial random distribution model  
 151 (dotted line), and the values of the normalized homogenization parameter  $\mu$  are all  
 152 close to 0, indicating the random distribution of all the elements at the near-atomic  
 153 scale [34-36]. Comparatively, the APT result of the  $\gamma$ -austenite in the aged steel (Fig.  
 154 3(a)) shows that the reconstructed intragranular  $\kappa$ -carbides are distributed along a  
 155 certain direction. The concentration profile in Fig. 3(b) shows the clear fluctuation of  
 156 the different elements traversing the  $\gamma$ -austenite and  $\kappa$ -carbides. The  $\kappa$ -carbides are  
 157 obviously rich in C and Al and poor in Fe, while the distributions of Mn and Cr  
 158 between the  $\gamma$ -austenite and  $\kappa$ -carbide are almost uniform. Thus, putting together the  
 159 HRSTEM and APT results clearly indicates that the chemical partitioning of solute

160 elements is unnecessary for the formation of the ordered  $\kappa$ -carbides.

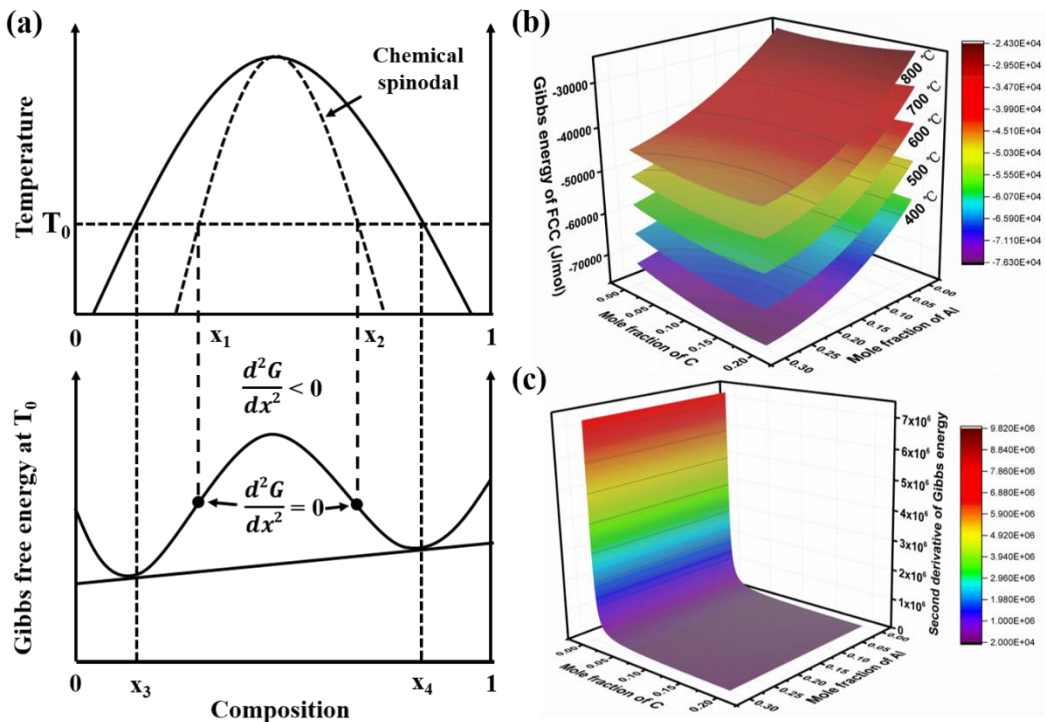


161

162 Fig. 3 APT characterization of  $\gamma$ -austenite in the aged steel: (a) reconstructed C map showing

163 intragranular  $\kappa$ -carbides with an iso-concentration surface at 6 at. % C; (b) 1 D concentration

164 profile generated by the 10 nm diameter virtual cylinder in (a).



165

166 Fig. 4 (a) Schematic phase diagram of miscibility gap and the corresponding free energy curve

167 [37]; (b) calculated Gibbs energy of FCC phase as a function of mole fractions of Al and C in

168 Fe-20Mn-9Al-3Cr-1.2C (wt. %) steel at the temperature range 400-800 °C; (c) calculated second  
169 derivative (curvature) of the Gibbs energy at 600 °C in (b).

170 Thermodynamically, the spinodal decomposition is a transformation without  
171 activation energy barrier and can result in a decreased total Gibbs energy [37]. When  
172 it occurs to the high temperature  $\gamma$ -austenite, the  $\gamma'$  and  $\gamma''$  phases form with the  
173 change of C and Al contents. Due to the same FCC crystal structure of the  $\gamma'$  and  $\gamma''$   
174 phases, the Gibbs energy of both phases will move along the same Gibbs  
175 energy-composition curve. To ensure the decreased total Gibbs energy of FCC phase,  
176 the Gibbs energy-composition curve has a negative curvature [37], i.e.  $\frac{d^2G}{dx^2} < 0$ , as the  
177 same as the composition range between  $x_1$  and  $x_2$  shown in Fig. 4 (a). A small  
178 composition fluctuation decreases its total free energy to give rise to the spinodal  
179 decomposition by up-hill diffusion. Outside this composition range, a small  
180 composition fluctuation results in an increase of the free energy, which makes the  
181 alloy unstable. To decrease the total free energy, an energy barrier must be overcome  
182 so that the nucleation and growth mechanism dominates. The calculated results (Fig.  
183 4(b)) show that the evolution trend of Gibbs energy of the FCC phase is the same at  
184 the large temperature range 400-800 °C. At each given temperature, the Gibbs energy  
185 decreases with increasing the mole fractions of Al and C, while its curvature remains  
186 always positive (the case of 600 °C shown in Fig. 4(c) and those of the other  
187 temperatures in [Supplementary](#)) ruling out the spinodal decomposition of  $\gamma \rightarrow \gamma' + \gamma''$ .  
188 It should be further noted that the calculated Gibbs energy in Fig. 4 (b) originates  
189 totally from the disordered FCC phase. The fact that the ordering reaction of  $\gamma'' \rightarrow$   
190  $L1_2$  phase has no contribution indicates that it is thermodynamically unfavorable.

191 According to the classical nucleation theory in solids [37], the minimum  
192 activation energy barrier for the  $\kappa$ -carbide precipitation in  $\gamma$ -austenite matrix is  
193 described as:

$$194 \quad \Delta G^* = \frac{16\pi\gamma_{\kappa/\gamma}^3}{3(\Delta G_V - \Delta G_S)^2} \quad (1)$$

195 where  $\gamma_{\kappa/\gamma}$  is interfacial energy between the  $\kappa$ -carbides and  $\gamma$ -austenite,  $\Delta G_V$  is  
196 chemical driving force of  $\kappa$ -carbides per unit volume and  $\Delta G_S$  is elastic strain energy.  
197 In equation (1), the interfacial energy and elastic strain energy can be further  
198 expressed as [38]:

$$199 \quad \gamma_{\kappa/\gamma} = \frac{\varepsilon(c-c_0)^2}{d^2} \quad (2)$$

$$200 \quad \Delta G_S = \frac{E\delta^2(c-c_0)^2}{1-\nu} \quad (3)$$

201 with lattice misfit  $\delta = \frac{a_\gamma - a_\kappa}{a_\kappa}$  (4)

202 where  $\varepsilon$  is pair interaction energy,  $c$  is nucleus composition,  $c_0$  is nominal composition,  
 203  $d$  is interface thickness,  $E$  is Young modulus,  $\nu$  is Poisson coefficient,  $a_\kappa$  and  $a_\gamma$  are  
 204 lattice parameters of the  $\kappa$ -carbides and  $\gamma$ -austenite, respectively.

205 At the initial stage of the  $\kappa$ -carbide formation, the fully coherent interface  
 206 between the  $\kappa$ -carbide and  $\gamma$ -austenite matrix is revealed in Fig. 1 (b). The interfacial  
 207 energy of  $\kappa$ -carbide precipitates in Fe-Mn-Al-C steel was calculated to be 0.025 J/m<sup>2</sup>  
 208 [29]. For comparison, it is much lower than the interfacial energy of 0.115 J/m<sup>2</sup>  
 209 necessary to form GP zones from the Al matrix in Al-Cu alloy [39]. The lattice misfit  
 210 ( $\delta$ ) between the  $\kappa$ -carbide and  $\gamma$ -austenite is estimated to about 0.27 % in term of the  
 211 HRSTEM-HAADF image in Fig. 1 (c), which results in the low  $\Delta G_S$  (measured lattice  
 212 parameters in [Supplementary](#)). More importantly, the nearly consistent composition  
 213 between the  $\kappa$ -carbides and  $\gamma$ -austenite matrix revealed by APT (see Fig. 2) indicates  
 214 that the critical nucleation composition of  $\kappa$ -carbide can be very close to that of the  
 215  $\gamma$ -austenite matrix, which makes the value of  $(c - c_0)$  close to zero. All the results  
 216 mean that there are both very low interfacial energy and elastic strain energy at the  
 217 initial stage of  $\kappa$ -carbide formation. Therefore, the activation energy barrier to the  
 218 nucleation of  $\kappa$ -carbides in  $\gamma$ -austenite matrix should be rather small. In addition, the  
 219 large undercooling, due to a high cooling rate of more than 10<sup>3</sup> K/s during the  
 220 near-rapid solidification [21], also increases the driving force for  $\kappa$ -carbide  
 221 precipitation [37, 40].

222 Table 1 Quantitative chemical compositions of  $\gamma$ -austenite matrix and  $\kappa$ -carbide precipitates  
 223 in the as-cast and aged steels obtained by APT analyses (in at. %).

Steel	Phase	Fe	Mn	Al	C	Cr
As-cast	$\gamma/\kappa$	58.42 ± 0.45	16.73 ± 0.11	17.50 ± 0.25	4.87 ± 0.25	2.48 ± 0.11
Aged	$\gamma$	60.41 ± 0.50	16.71 ± 0.13	15.95 ± 0.27	4.39 ± 0.26	2.54 ± 0.07
	$\kappa$	56.00 ± 0.29	16.43 ± 0.12	18.22 ± 0.22	6.37 ± 0.25	2.45 ± 0.17

224 Further, density functional theory calculations [41, 42] suggest that the Fe, Mn  
 225 and Cr atoms are usually considered to be located at the face center positions of the  
 226 ideal (Fe, Mn)<sub>3</sub>AlC lattice. Assuming that such positions in the initially formed  
 227  $\kappa$ -carbide are completely occupied and as shown in Table 1, the occupancy rates of Al  
 228 and C atom positions are determined to be 67.6 % and 18.8 %, respectively. This  
 229 indicates that there is a large amount of quenched-in vacancies in the  $\kappa$ -carbides  
 230 effectively promoting nucleation by increasing diffusion rates or relieving misfit  
 231 strain energies [37]. Simultaneously, the presence of vacancies is a critical way to  
 232 achieve ordering structures in non-stoichiometric phases [37]. The formation of an

233 ordered structure by nucleation only requires the short-range movement of atoms in a  
234 crystal lattice, which is much easier to achieve than the spinodal decomposition [43].

235 With the growth of  $\kappa$ -carbides after the aging treatment, their composition  
236 gradually approaches the equilibrium composition with the higher contents of Al and  
237 C. The interfacial energy and elastic strain energy also increase by the increased  
238 composition difference ( $c - c_0$ ) between the  $\kappa$ -carbides and  $\gamma$ -austenite matrix (see  
239 Table 1), and the increased lattice misfit ( $\delta$ ) of 2.27 % obtained by HRSTEM-HAADF  
240 image (Fig. 1 (f)) and equation (4). The increased lattice misfit ( $\delta$ ) resulted from the  
241 partitioning of Al and C to the  $\kappa$ -carbides [4, 7, 12]. This indicates that nucleation of  
242 the equilibrium  $\kappa$ -carbides directly in the  $\gamma$ -austenite matrix is difficult. Therefore,  
243 there must be a change in composition and associated crystal structure accompanying  
244 with the nucleation and growth process.

245 In summary, the formation mechanism of the intragranular  $\kappa$ -carbide in  
246  $\gamma$ -austenite of the austenite-based Fe-20Mn-9Al-3Cr-1.2C low-density steel was  
247 revisited in terms of (HR)STEM, APT and thermodynamic calculation. It was  
248 experimentally observed that the  $\kappa$ -carbide precipitates of 2-3 nm in particle size were  
249 homogeneously distributed in  $\gamma$ -austenite of the as-cast steel. They corresponded to the  
250 ordered  $L'1_2$  structure without elemental partitioning at near-atomic scale. The  
251 thermodynamic calculations indicated that the Gibbs energy of the FCC phase always  
252 had a positive curvature with the variable contents of Al and C in the temperature  
253 range 400-800 °C. These results clearly show that the formation of the intragranular  
254  $\kappa$ -carbide in the as-cast and aged steels obeys the nucleation and growth mechanism  
255 rather than the well-known spinodal decomposition-ordering mechanism. The similar  
256 lattice structure, same composition and complete coherency between the  $\gamma$ -austenite  
257 and  $\kappa$ -carbide resulted in an extremely low nucleation barrier. With the growth of  
258  $\kappa$ -carbides after aging, their composition tended to be stable, which increased the  
259 composition fluctuation between the  $\gamma$ -austenite and  $\kappa$ -carbide.

260

## 261 **Acknowledgements**

262 This work was financially supported by the National Natural Science Foundation  
263 of China (No. 51974184), National MCF Energy R&D Program of China (No.  
264 2018YFE0306102). Jianlei Zhang was grateful for his visiting Ph.D. project  
265 supported by the China Scholarship Council (Grant No. 201906890053). The authors  
266 would like to express sincere thanks to the use of atom probe tomography (APT) in  
267 the Instrumental Analysis & Research Center at Shanghai University. The TEM  
268 facility in Lille, France, is supported by the Conseil Regional du Nord-Pas de Calais  
269 and the European Regional Development Fund (ERDF).

270 **Reference**

- 271 [1] S.P. Chen, R. Rana, A. Haldar, R.K. Ray, *Prog. Mater. Sci.* 89 (2017) 345-391.
- 272 [2] F. Herrig, D. Music, H. Rueß, A.L. Ravensburg, P.J. Pöllmann, J.M. Schneider, *Scr.*  
273 *Mater.* 153 (2018) 49-53.
- 274 [3] J. Moon, S.J. Park, J.H. Jang, T.H. Lee, C.H. Lee, H.U. Hong, D.W. Suh, S.H.  
275 Kim, H.N. Han, B.H. Lee, *Scr. Mater.* 127 (2017) 97-101.
- 276 [4] Z.W. Wang, W.J. Lu, H. Zhao, J.Y. He, K. Wang, B.C. Zhou, D. Ponge, D. Raabe,  
277 Z.M. Li, *Acta Mater.* 198 (2020) 258-270.
- 278 [5] M.J. Yao, E. Welsch, D. Ponge, S.M.H. Haghighat, S. Sandlöbes, P. Choi, M.  
279 Herbig, I. Bleskov, T. Hickel, M. Lipinska-Chwalek, P. Shanthraj, C. Scheu, S.  
280 Zaefferer, B. Gault, D. Raabe, *Acta Mater.* 140 (2017) 258-273.
- 281 [6] E. Welsch, D. Ponge, S.M.H. Haghighat, S. Sandlöbes, P. Choi, M. Herbig, S.  
282 Zaefferer, D. Raabe, *Acta Mater.* 116 (2016) 188-199.
- 283 [7] M.J. Yao, P. Dey, J.B. Seol, P. Choi, M. Herbig, R.K.W. Marceau, T. Hickel, J.  
284 Neugebauer, D. Raabe, *Acta Mater.* 106 (2016) 229-238.
- 285 [8] S.C. Tjong, *Mater Charact* 24(3) (1990) 275-292.
- 286 [9] J.L. Zhang, C.H. Hu, Y.H. Zhang, J.H. Li, C.J. Song, Q.J. Zhai, *Mater. Des.* 186  
287 (2020) 108307.
- 288 [10] Y. Sutou, N. Kamiya, R. Umino, I. Ohnuma, K. Ishida, *ISIJ Int.* 50(6) (2010)  
289 893-899.
- 290 [11] A.P. Bentley, *J Mater Sci Lett* 5(9) (1986) 907-908.
- 291 [12] L.N. Bartlett, D.C. Van Aken, J. Medvedeva, D. Isheim, N.I. Medvedeva, K.  
292 Song, *Metall Mater Trans A* 45(5) (2014) 2421-2435.
- 293 [13] Y.F. Feng, R.B. Song, Z.Z. Pei, R.F. Song, G.Y. Dou, *Met. Mater. Int.* 24(5)  
294 (2018) 1012-1023.
- 295 [14] W.C. Cheng, *JOM* 66(9) (2014) 1809-1820.
- 296 [15] K. Sato, K. Tagawa, Y. Inoue, *Mater. Sci. Eng. A* 111 (1989) 45-50.
- 297 [16] W.C. Cheng, C.Y. Cheng, C.W. Hsu, D.E. Laughlin, *Mater. Sci. Eng. A* 642  
298 (2015) 128-135.
- 299 [17] K.H. Han, J.C. Yoon, W.K. Choo, *Scr. Metar.* 20(1) (1986) 33-36.
- 300 [18] K. Sato, K. Tagawa, Y. Inoue, *Scr. Metar.* 22(6) (1988) 899-902.
- 301 [19] C.W. Kim, M. Turner, J.H. Lee, H.U. Hong, J. Moon, S.J. Park, J.H. Jang, C.H.  
302 Lee, B.H. Lee, Y.J. Lee, *J. Alloys Compd.* 775 (2019) 554-564.
- 303 [20] Y. Yang, J.L. Zhang, C.H. Hu, Z.P. Luo, Y.H. Zhang, C.J. Song, Q.J. Zhai, *Mater.*  
304 *Sci. Eng. A* 748 (2019) 74-84.
- 305 [21] L.B. Liu, C.M. Li, Y. Yang, Z.P. Luo, C.J. Song, Q.J. Zhai, *Mater. Sci. Eng. A*  
306 679 (2017) 282-291.
- 307 [22] J. Barthel, *Ultramicroscopy* 193 (2018) 1-11.
- 308 [23] J.B. Seol, D. Haley, D.T. Hoelzer, J.H. Kim, *Acta Mater.* 153 (2018) 71-85.
- 309 [24] J.B. Seol, H.S. Park, C.G. Park, *Microsc. Microanal.* 22(S3) (2016) 704-705.
- 310 [25] W.S. Zheng, S. He, M. Selleby, Y.L. He, L. Li, X.G. Lu, J. Ågren, *CALPHAD* 58  
311 (2017) 34-49.

312 [26] W.S. Zheng, X.G. Lu, H.H. Mao, Y.L. He, M. Selleby, L. Li, J. Ågren,  
313 CALPHAD 60 (2018) 222-230.  
314 [27] W.S. Zheng, H.H. Mao, X.G. Lu, Y.L. He, L. Li, M. Selleby, J. Ågren, J. Alloys  
315 Compd. 742 (2018) 1046-1057.  
316 [28] J.O. Andersson, T. Helander, L. Höglund, P.F. Shi, B. Sundman, CALPHAD 26(2)  
317 (2002) 273-312.  
318 [29] W.S. Zheng, KTH Royal Institute of Technology, 2018.  
319 [30] K.H. Yang, W.K. Choo, Philos Mag Lett 62(3) (1990) 221-226.  
320 [31] J.B. Seol, J.W. Bae, J.G. Kim, H. Sung, Z.M. Li, H.H. Lee, S.H. Shim, J.H. Jang,  
321 W.S. Ko, S.I. Hong, H.S. Kim, Acta Mater. 194 (2020) 366-377.  
322 [32] S.D. Kim, J.Y. Park, S.J. Park, J.H. Jang, J. Moon, H.Y. Ha, C.H. Lee, J.Y. Kang,  
323 J.H. Shin, T.H. Lee, Sci. Rep. 9(1) (2019) 1-13.  
324 [33] D.E. Jesson, S.J. Pennycook, Proc Roy Soc Lond Math Phys Sci 449(1936)  
325 (1995) 273-293.  
326 [34] M.J. Yao, K.G. Pradeep, C.C. Tasan, D. Raabe, Scr. Mater. 72-73 (2014) 5-8.  
327 [35] H. Yuan, M.H. Tsai, G. Sha, F. Liu, Z. Horita, Y.T. Zhu, J.T. Wang, J. Alloys  
328 Compd. 686 (2016) 15-23.  
329 [36] Z.M. Li, F. Körmann, B. Grabowski, J. Neugebauer, D. Raabe, Acta Mater. 136  
330 (2017) 262-270.  
331 [37] D.A. Porter, K.E. Easterling, M.Y. Sherif, Phase transformations in metals and  
332 alloys, third ed., CRC press, 2009.  
333 [38] T. Philippe, D. Blavette, Philos Mag 91(36) (2011) 4606-4622.  
334 [39] K.C. Russell, H.I. Aaronson, J. Mater. Sci. 10 (1975) 1991-1999.  
335 [40] J.B. Seol, D. Raabe, P. Choi, H.S. Park, J.H. Kwak, C.G. Park, Scr. Mater. 68(6)  
336 (2013) 348-353.  
337 [41] J.Y. Noh, H. Kim, J Korean Phys Soc 62(3) (2013) 481-485.  
338 [42] J. Moon, H.Y. Ha, K.W. Kim, S.J. Park, T.H. Lee, S.D. Kim, J.H. Jang, H.H. Jo,  
339 H.U. Hong, B.H. Lee, Y.J. Lee, C. Lee, D.W. Suh, H.N. Han, D. Raabe, C.H. Lee, Sci.  
340 Rep. 10(1) (2020) 1-10.  
341 [43] G.B. Viswanathan, R. Banerjee, A. Singh, S. Nag, J. Tiley, H.L. Fraser, Scr.  
342 Mater. 65(6) (2011) 485-488.